CHALMERS

Uncertainty Models for Reverberation Chambers

An adaptation of an uncertainty model for a new measurement environment at National Institute of Standards and Technology, Boulder, USA

Master of Science Thesis in the Master's Programme Wireless and Photonics

ERIK ENGVALL

Department of Signals and Systems
CHALMERS UNIVERSITY OF TECHNOLOGY
Göteborg, Sweden 2012

MASTER'S THESIS

Uncertainty Models for Reverberation Chambers

An adaptation of an uncertainty model for a new measurement environment at National Institute of Standards and Technology, Boulder, USA

Master of Science Thesis in the Master's Programme Wireless and Photonics

ERIK ENGVALL

Department of Signals and Systems
CHALMERS UNIVERSITY OF TECHNOLOGY
Göteborg, Sweden 2012

Uncertainty Models for Reverberation Chambers
An adaptation of an uncertainty model for a new measurement environment at National Institute of Standards and Technology, Boulder, USA

Master of Science Thesis in the Master's Programme Wireless and Photonics

ERIK ENGVALL

Examiner: Professor Per-Simon Kildal

Department of Signals and Systems
Chalmers University of Technology
SE-412 96 Göteborg
Sweden
Telephone: + 46 (0)31-772 1000

Cover:
Dual ridge horn antenna pointed at mode stirrer in the NIST reverberation chamber.

Preface

In this study an evaluation of the uncertainty of power measurements in two different reverberation chambers has been performed. Experiments have been carried out between August 2011 and June 2012. Seven months were spent as a guest researcher at the National Institute for Standards and Technology (NIST) in Boulder, Colorado, USA. In this thesis the results from my work at both NIST and the Antenna Group Chalmers is presented. Professor Per-Simon Kildal has been the examiner and tutor at Chalmers. At NIST my work was supervised by Professor Christopher L. Holloway.

Acknowledgements

I would like to thank my supervisors Professor Per-Simon Kildal and Professor Christopher L. Holloway for the chance of working with this thesis and for the guidance they have provided. A special thanks goes out to Ryan Pirkl and Xiaoming Chen for sharing their expertise regarding reverberation chambers and also for their patience and encouraging words at all times. I would also like to mention John Ladbury for all the experimental advice at the NIST lab.

I also want to thank my family, my friends from physics at Chalmers and Linnea for supporting me throughout my thesis work.

Göteborg, June 2012

Erik Engvall

Uncertainty Models for Reverberation Chambers

An adaptation of an uncertainty model for a new measurement environment at National Institute of Standards and Technology, Boulder, USA

Master of Science Thesis in the Master's Programme Wireless and Photonics
ERIK ENGVALL
Department of Signals and Systems
Chalmers University of Technology

Abstract

The Reverberation Chamber has become a good alternative for over-the-air (OTA) testing of small antennas. This thesis deals with the uncertainty of these types of measurements in two different reverberation chambers (RC's). A procedure for measuring the uncertainty based on the standard deviation of nine different antenna orientations in the RC has been used.

At Chalmers University of Technology an upgrade of a RC model from Bluetest is evaluated in terms of average mode bandwidth, average K-factor and uncertainty. It is found that the uncertainty has become better, to a value at about 0.14 dB for frequencies above 1.5GHz. The amount of direct coupling, shown by the average K-factor, has also decreased.

At NIST, Boulder, the influence on the uncertainty of introducing a platform stirrer has been evaluated. This has lowered the uncertainty from 0.5 dB to 0.3 dB. The platform does not have a rotation feature and introduces some correlation which affects the uncertainty measurement negatively. When replacing this first platform with a rotational platform the uncertainty drops down to 0.15 dB and gives a flat frequency response without any correlation effects.

A uncertainty model has been developed by Prof. Kildal's group at Chalmers University of Technology. The model uses the average K-factor to predict the level of uncertainty in the RC's. The agreement of the model with experimental values is evaluated for both RC's and the model is found to work well in both cases.

For high number of stirrer positions the measured uncertainty gets saturated at a certain level. To account for this a modification to the model built on the mechanical bandwidth of the chamber, Bmech, has been made. For a fixed average K-factor a mechanical bandwidth of 20MHz is found to fit the measured data well for the Chalmers RC. This limits the model and can follow the saturation for high number of stirrer positions.

Contents

1 Introduction

The development of products using wireless technology has increased rapidly over the recent years. Increasing demands of data capacity and more reliable networks has led to an expansion of existing technology into new areas, for example multiple input multiple output (MIMO) systems [1]. In order to meet the industry's demands for a realistic test environment for the wireless devices the reverberation chamber (RC) provides a good alternative [2].

The reverberation chamber is a shielded room with metal walls with one or more rotating metallic paddles (stirrers) inside. Traditionally the RC has been used for electromagnetic compatibility (EMC) testing of electrical devices [3], but it has developed into a test facility for characterizing small antennas [4]. It can be used for measuring radiation efficiency, total radiated power, diversity gain, maximum available capacity of MIMO systems, receiver sensitivity and throughput [5].

The walls of the RC are highly reflective for electromagnetic radiation and gives an environment rich in electromagnetic modes [6]. This gives a multipath environment similar to what a small antenna (in for example a mobile phone) is exposed to outdoors [7]. The rotating paddles allows for changing the electromagnetic modes over time, resulting in a known statistical distribution of the transfer functions.

In characterizing the chamber, the degree of the line-of-sight (LOS) component present in the multipath environment is important. It is quantified by the average K-factor and can be found through the measured S-parameters [8]. This factor will be important to estimate the uncertainty of RC measurements. Another important factor is the average mode bandwidth, which can be used as a measure of the amount of loading in the chamber [9].

This report will investigate the uncertainty afforded by two different RC's, one located at Chalmers University of Technology (CTH) in Sweden and one located at National Institute of Standards and Technology (NIST), Boulder, USA. The standard deviation of the transfer functions for different antenna positions in the RC is used as a measure of the achievable uncertainty of measurements in the chamber.

Prof. Kildal's research group at Chalmers University of Technology has developed a theoretical model for measurement uncertainty [10] and the subject of this report is to evaluate and possibly extend this model for a RC different than the one used at Chalmers.

2 Theory

2.1 The Reverberation Chamber

The reverberation chamber (RC) is a room with metallic walls. These walls provide shielding from the outside and are electromagnetically reflective from the inside. A radiating antenna in the RC will excite modes near the operating frequency and create a statistical spatial distribution of field minimum and maximum. The induced voltage on a receiving antenna placed in the RC will not coincide with the min/max positions due to antenna characteristics such as radiation pattern and polarization. Thus the induced voltage can be considered to be a random variable [11].

The induced voltage on a receiving antenna can be varied by mechanical stirring, i.e movement of metal plates in the RC. This will give a statistical variation even though the antenna remains in a fixed position. If the chamber is electrically large and stirring is applied, the electric and magnetic fields will ideally follow a complex Gaussian distribution [12]. This means that the induced voltage on the receiving antenna also will be complex Gaussian.

A complex Gaussian distribution with zero mean of the voltage means that the absolute value will be Rayleigh distributed and the received power (absolute value squared) will be exponential distributed [11].

There may also exist a constant field component that is unaffected by the mechanical stirring. This component can be used to generate a Rician environment, instead of the Rayleigh environment [5].

2.2 Basic Principles for the RC in terms of S-Parameters

In this section a theoretical formulation of the RC will be presented in terms of S-parameters. S_{11} and S_{22} are the reflections from the antenna ports while transmitting into the RC, S_{21} is the transmission between the antennas (the channel) characterizing the path in the chamber. The notation used is an adaptation from the signal processing field also used in [10].

The S_{11} parameter can be divided into two parts (eq 1). One antenna contribution S_{11}^a and one channel contribution H_{11}^c, where S_{11}^a is the average of S_{11} for all stirrer positions. This can be done analogously for S_{22}.

$$S_{11} = S_{11}^a + H_{11}^c \tag{1}$$

The same can be done for S_{21} (eq 2). One deterministic part H_{21}^d (LOS component) and one statistic part H_{21}^c (NLOS or multipath component), where H_{21}^d is the average of S_{21} for all stirrer positions.

$$S_{21} = H_{21}^d + H_{21}^c \tag{2}$$

If polarization or platform stirring is used the averaging of S_{11} and S_{21} is not possible. The direct coupling will vary in that case. This can be solved by using an average Rician K-factor first presented in [8], also discussed in Section 2.4.

2.2.1 Line of Sight Contribution (LOS)

The direct coupling is described by Friis' formula [13], where the gains are measured in the same direction, eq 3. The direct coupling can be reduced by pointing the antennas in different directions and thereby reducing the gains. It can also be reduced by introducing polarization and platform stirring.

$$G_{direct} = |H_{21}^d|^2 = \left(\frac{\lambda}{4\pi r}\right)^2 G_t G_r \tag{3}$$

2.2.2 Multipath Contribution (NLOS)

The multipath component in a RC can be described by Hill's formula [14], eq 4. Here the important factors are the antenna radiation efficiency and not their gains. Δf is the average mode bandwidth (see section 2.5) and V is the chamber volume.

$$G_{chamber} = |H_{21}^c|^2 = P_r/P_t = \frac{c^3 e_{rad1} e_{rad2}}{16\pi^2 V f^2 \Delta f} \tag{4}$$

Measurements in the RC are based on the fact that, for a given chamber, frequency and loading configuration, the average power transfer function is proportional to the total radiation efficiency, as shown in Hill's formula (eq 4). This is true if the antennas and lossy objects in the chamber contribute negligibly to the average mode bandwidth. $\Delta f_{antenna}, \Delta f_{object} << \Delta f$.

Hills formula requires a large number of excited modes and negligible direct coupling (LOS) [15]. To have low direct coupling antennas must be placed away from walls, at least $\frac{\lambda}{2}$ away [3].

2.3 The Reference Transfer Function

When doing power measurements in the RC, a reference transfer function is calculated from the S-parameters. S-parameters are a measure of voltage, which needs to be squared to represent power (from Joule's and Ohm's laws). The stirring in the chamber provides a statistical distribution of the power. The average over this stirring distribution is used as the reference transfer function [16]. However the parameter S_{21} is not just the paths between the two antennas; S_{21} is also affected by the antennas' radiation efficiencies (here denoted e_{rad} and e_{ref}). This has to be compensated for as in equation 5.

$$G_{ref,net} = \frac{\overline{|S_{21}|^2}}{e_{rad} \cdot e_{ref}} \tag{5}$$

The radiation efficiencies can be measured very accurately in an anechoic camber. If we instead assume lossless antennas the total radiation efficiency becomes equal to the mismatch factor, as in equation 6 [17]. Enabling the use of measured S-parameters from the RC.

$$e_{ref} = 1 - |\overline{S_{22}}|^2 \tag{6}$$

e_{rad} can be found in an analogous way. Using these relations equation 5 can be rewritten as in equation 7.

$$G_{ref,net} = \frac{\overline{|S_{21}|^2}}{(1 - |\overline{S_{11}}|^2)(1 - |\overline{S_{22}}|^2)} \tag{7}$$

2.4 Average K-Factor in the RC

The K-factor is a measure of the amount of direct coupling in the chamber relative to the multipath component provided by the chamber. When the RC is loaded this will affect the multipath part but leave the direct coupling unaffected [5]. Multipath environments with different characteristics can be created by providing different loading in the chamber. The K-factor can be used to characterize these

multipath environments. It can be calculated as the power of the LOS part (eq 3) relative to the average power of the NLOS part (eq 4), resulting in eq 8. In this equation D_t and D_r are the directivity of the transmit and receive antennas.

$$K = \frac{G_{direct}}{G_{chamber}} = \frac{V}{r^2}\frac{\Delta f}{c} D_t D_r \tag{8}$$

The K-factor can also be determined by measuring S_{21} and calculating $H^d_{21,iLOS}$ and $|H^c_{21}|^2$ as in eq 9 and 10 [18].

$$H^d_{21,iLOS} = \left\{ \frac{1}{M_{NLOS}} \sum_{M_{NLOS}} S_{21} \right\} \tag{9}$$

$$|H^c_{21}|^2 = \frac{1}{M_{NLOS} M_{LOS}} \sum_{M_{NLOS} M_{LOS}} |H^c_{21,iLOS}|^2 \tag{10}$$

In eq 10 $H^c_{21,iLOS}$ is the deviation from the mean of S_{21} over all platform positions, as in eq 11.

$$H^c_{21,iLOS} = S_{21} - \overline{S_{21,iLOS}} \tag{11}$$

Looking at equation 8 we see that K varies with position in the chamber, therefor it is convenient to use an averaged K_{av} over all positions of the platform [8] (a test of this averaging is performed in section 4.2.4), resulting in K_{av} as in equation 12 . This approach is used in this report.

$$K_{av} = \frac{\overline{|H^d_{21}|^2}}{\overline{|H^c_{21}|^2}} \tag{12}$$

2.5 Average Mode Bandwidth, Δf, as a Chamber Characteristic

The mode bandwidth is defined as the frequency range where the excited power of a particular mode, centered at f_0, is larger than half the excited power at f_0. In other words, it is the 3 dB bandwidth of the exited power of a specific mode [16].

The average mode bandwidth, Δf, is the average 3 dB bandwidth of all modes excited at f_0.

The average mode bandwidth originates from losses in the RC. Hill defined in [14] that these can be described by Δf_{wall} due to finite conductivity in the walls, Δf_{obj} due to absorbing objects in the RC, Δf_{slot} due to aperture leakage and Δf_{ant} due to the antennas present in the RC. Expressions for these contributions are given in equations 13-16, rewritten as in [9]. These contributions are additive and their sum equals the total Δf (eq 17). Δf_{obj} is the dominant contribution to the average mode bandwidth at the frequencies of interest [9].

$$\Delta f_{wall} = \sum_{walls} \frac{2A}{3V} \sqrt{\frac{c\rho f}{\pi \eta}} \tag{13}$$

$$\Delta f_{obj} = \sum_{objects} \frac{c}{2\pi V} \sigma_a \tag{14}$$

$$\Delta f_{slot} = \sum_{slots} \frac{c}{4\pi V} \sigma_l \tag{15}$$

$$\Delta f_{ant} = \sum_{antennas} \frac{c^3 e_{rad}}{16\pi^2 V f^2} \tag{16}$$

$$\Delta f = \Delta f_{wall} + \Delta f_{slot} + \Delta f_{obj} + \Delta f_{ant} \tag{17}$$

The dominant factor, Δf_{obj}, depends on objects inside the chamber (loading). The loss from these objects are fairly flat over the frequency of operation of these types of RC's. Looking at the Δf_{obj} in equation 14 there is no frequency dependence present. This being the dominant part of Δf means that Δf's dependence on frequency is small. The Q-value used in [14] is defined as $Q = f/\Delta f$ and thus has a stronger frequency dependence than Δf. This makes the average mode bandwidth less sensitive to frequency in a RC and suitable for use as a chamber characteristic.

Using Δf as a loading characteristic and K_{av} as a fading characteristic gives a good picture of the environment in the RC. Δf can also be calculated from measurements by using Hill's formula (eq 4) and the transfer function $G_{ref,net}$ (eq 7). The resulting formula is shown in equation 18 and this is how Δf is calculated throughout this report.

$$\Delta f = \frac{c^3}{16\pi^2 V f^2 G_{ref,net}} \tag{18}$$

2.6 Theoretical Model for the Uncertianty of a RC

Prof. Kildal's group at Chalmers University of Technology has developed a model for the uncertainty in a RC. A brief theoretical explanation is given here, for the full derivation see [10].

As seen in section 2.2 there are two separate, independent Gaussian processes in play. The random LOS process that is the stirred (polarization and platform) direct coupling and the random NLOS process that is the mode stirring.

The NLOS part has the standard deviation $\sigma_{NLOS} = 1/\sqrt{N_{ind}}$ which means $N_{ind} = 100$ for a 0.5 dB limit. N_{ind} can be expressed as $N_{ind} = M_{plate}M_{pf,ind}M_{ant}$. The number of independent samples for the platform, $M_{pf,ind}$, can be bound as in the Chalmers case. In the NIST case it is not bound and $M_{pf,ind}$ is simply the number of platform positions. The bound state can be calculated by eq 19 [10]. R is the radius of the platform and α is a tuning parameter.

$$M_{pf,ind} = max\{8, min[M_{pf}, \frac{2Rsin(2\pi/M_{pf})M_{pf}}{\alpha\lambda/2}]\} \tag{19}$$

The LOS part has a similar standard deviation $\sigma_{LOS} = 1/\sqrt{N_{LOS,ind}}$. Here there are no bound conditions and the expression for $N_{LOS,ind}$ is simply $N_{LOS,ind} = M_{LOS} = M_{pf}M_{ant}$. In the upgraded RTS chamber at Chalmers the wall antennas has been located on a cube behind a metal screen. This reduces the space diversity and makes the antennas look as only one antenna for the LOS case, that is M_{ant} should be set to 1 for this part.

The final formula for the RC uncertainty in an average power estimate when accounting for the K-factor is expressed as in eq 20 [10]. The standard deviation has been weighted with the average K-factor to account for the relative distribution of the two contributions.

$$\sigma = \sqrt{(\sigma_{NLOS})^2 + K_{av}^2(\sigma_{LOS})^2}/\sqrt{1 + K_{av}^2} \tag{20}$$

2.6.1 Number of Independent Samples as a Limitation for the Uncertainty Model

If the number of independent samples, N_{ind}, would be possible to increase towards infinity the model predicts a standard deviation of zero. The expression for N_{ind} in section 2.6 does not have a limit of how many samples that can be used. An increase in number of samples just pushes the standard deviation further down.

In a measurement situation the standard deviation goes to a certain value, other than zero, when the number of samples increases. If, for example, two stirrer positions are very close to each other in terms of wavelengths the modes in the RC might not change enough. This means that adding more samples not necessarily gives more information, they may be correlated.

There is a limit to how many samples that can be considered independent for a certain measurement equipment. This number of independent samples that can be achieved in a RC is related to the number of modes as in equation 21 [19].

$$N_{ind,1} = 8N_{mode} \tag{21}$$

The number of possible excited modes can be calculated through a modification of Weyl's formula [20] as in equation 22. It is a function of the volume of the RC, by the average mode bandwidth, by the frequency and by the parameter B_{mech}, called the mechanical bandwidth. B_{mech} is not yet fully determined but it is influenced by stirring sequences, by the shape of the mode stirrers and by the shape of the RC.

$$N_{mode} = \frac{Vf^2 8\pi}{c^3}(B_{mech} + \Delta f) \tag{22}$$

In order to deal with this saturation a modification of the model for the uncertainty was implemented. Before we had the number of independent samples for the NLOS part as in equation 23 and now a combination of equation 21 and 23 are used, equation 24. Here *min* denotes the choice of the smallest of the two numbers in the parentheses, giving a limitation for high numbers of stirrer positions.

$$N_{ind,2} = M_{plate}M_{pf,ind}M_{ant} \tag{23}$$

$$N_{ind,3} = min\left(N_{ind,2}, N_{ind,1}\right) = min\left(M_{plate}M_{pf,ind}M_{ant}, 8N_{mode}\right) \tag{24}$$

This new, limited $N_{ind,3}$ is used as input to the model in equation 20.

2.7 Correlation Coefficient for Alternative Uncertainty Measurement

Pearson's correlation coefficient is defined as the covariance between the two variables divided by the standard deviations of the respective variables [21]. A general

expression is given in equation 25.

$$\rho_{X,Y} = \frac{cov(X,Y)}{\sigma_X \sigma_Y} = \frac{E[(X-\mu_X)(Y-\mu_Y)]}{\sigma_X \sigma_Y} \tag{25}$$

In this application the correlation coefficient is used as a measure of how much of the same signal two antennas have received. If two identical antennas are in the exact same position they will pick up the same signal, hence the correlation coefficient ρ equals 1. When applying Pearson's correlation coefficient to a sample, here the complex S-parameters, the equation takes the form as in equation 26 [21].

$$\rho = \left| \frac{\sum_{k=1}^{N} \Big(S_{21}(k) - \langle S_{21} \rangle \Big) \Big(S_{31}(k) - \langle S_{31} \rangle \Big)^*}{\sqrt{\sum_{k=1}^{N} |S_{21}(k) - \langle S_{21} \rangle|^2 \sum_{k=1}^{N} |S_{31}(k) - \langle S_{31} \rangle|^2}} \right| \tag{26}$$

3 Method for Uncertainty Measurements

Inside the RC we have a rich isotropic environment with the angle of arrival of incident plane waves on the AUT uniformly distributed over a unit sphere. From this it follows that there should be no difference in the induced voltage on the AUT when pointed in different directions and placed in different positions in the RC. In [8] it is proposed to measure the power transferred by use nine different positions and orientations of a calibration antenna. From these nine measurements the net reference transfer functions (eq. 7) is calculated and the standard deviation of these functions is interpreted as the uncertainty of the RC for power measurements. The uncertainty depends on characteristics such as the frequency, stirrer shapes and movement, polarization stirring, chamber size and loading of the chamber.

This report evaluates the uncertainty of over-the-air (OTA) measurements in two reverberation chambers.

Uncertainty measurements of the Bluetest HP chamber are presented in [19]. Now Bluetest has a new model (RTS60) with reduced direct coupling and more efficient mode stirring. This report will investigate if and how much the uncertainty is improved with these upgrades. It is also of interest to see if the uncertainty model developed at Chalmers (section 2.6) is valid for this new RC as well. The model will also be tested for a different RC manufactured by ETS-Lindgren, located at NIST, Boulder, Colorado. The uncertainty of this RC is reported in [22]. In this report platform stirring will be added to further improve the uncertainty.

As an additional study of the uncertainty this report will investigate the corre-

lation of a two antenna system in the RC at NIST. In the same way as for the power measurement above the standard deviation of nine measurements will be interpreted as the uncertainty for the chamber.

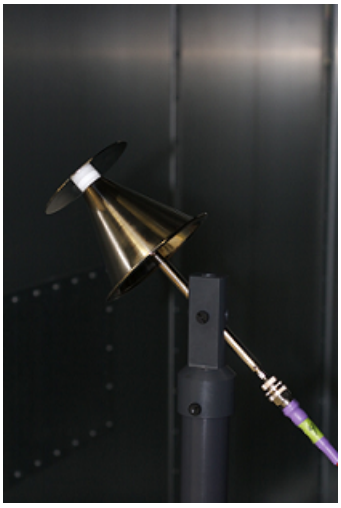

Figure 1: Discone antenna used as calibration antenna for the uncertainty measurements both at Chalmers and at NIST. Working at 500 MHz to 3 GHz.

3.1 Bluetest RTS RC at Chalmers

Uncertainty measurements has been performed for two different reverberation chambers. In this section the test specifications for the Bluetest RC at Chalmers are presented.

3.1.1 Equipment

The RC at Chalmers is provided by Bluetest. It is called RTS60 and has the dimentions 1.8 m x 1.7 m x 1.2 m. The stirring is performed by two rectangular plates that move along one wall and the ceiling, i.e. not rotating paddles as traditionally used.

The antenna under test (AUT) is placed on a circular turntable that can rotate to provide platform stirring. This enables a large number of independent samples, with more combinations of stirrer positions. The rotation of the AUT also provides a form of averaging of polarization directions when completing a whole revolution. This reduces the effect of the AUT's radiation pattern [10].

Three chamber antennas are mounted inside the RTS RC. These have orthogonal polarizations to enable polarization stirring. The AUT is a discone antenna from Bluetest (figure 1) with a frequency range of 650 MHz to 3.5 GHz.

To load the chamber a water filled head phantom was used together with three

cylinders containing absorbing material.

3.1.2 Measurement setup

The nine positions for the uncertainty measurement were chosen as vertical antenna, horizontal antenna pointing tangential to the circular platform and horizontal antenna pointing radially to the circular platform. These three orientations were carried out at three different heights: 55 cm, 75 cm and 95 cm above the RC floor.

The frequency band of the measurements was 500 MHz to 3 GHz. Due to limitations in the software, one measurement point for every two MHz was used.

The plate stirrers moved through their whole range over 20 positions. The number of positions for the rotational platform was 25, giving a total of $20 \cdot 25 = 500$ stirrer configurations.

Three different loading cases were measured in order to create environments with different average K-factors and different Δf. No damping is referred to as $Load0$, damping with only the head phantom is referred to as $Load1$ and damping with the head phantom plus three cylinders is referred to as $Load2$.

3.2 ETS RC at NIST

The second measurement set was performed in the reverberation chamber at NIST, Boulder. Here the test specifications for the ETS RC at NIST are presented.

3.2.1 Equipment

The RC at NIST is provided by ETS. It has the dimensions 4.3 m x 3.8 m x 2.9 m and is considerably larger than the RC at Chalmers. The stirring is performed by two large rotational paddles (figure 2), one vertical and one horizontal.

To provide platform stirring two methods were used. First the reference antenna was placed on a positioner able to move in the x-y-plane (figure 3). This moved the antenna through 9 positions during one measurement. Here no rotation of the AUT is possible, the AUT will point in the same direction for all points on the positioner. The positions are located on a square grid with 25 cm between each point along the x- and y-directions.

The second platform stirring was a simulation of a rotational platform similar to

the one in the RTS RC at Chalmers case. The AUT was turned manually through 8 points separated by 45°, instead of using the XY positioner. This distributes the polarizations in one plane and reduces some of the polarization imbalances.

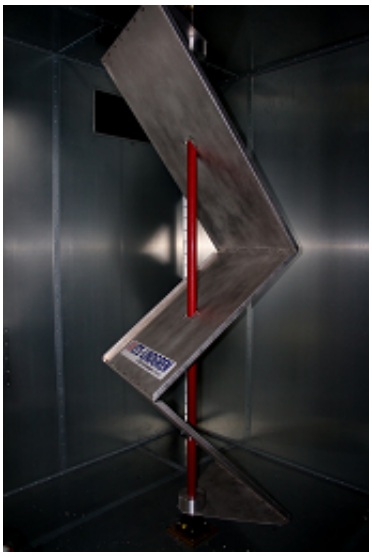

Figure 2: Vertical paddle for mode stirring inside the ETS RC at NIST.

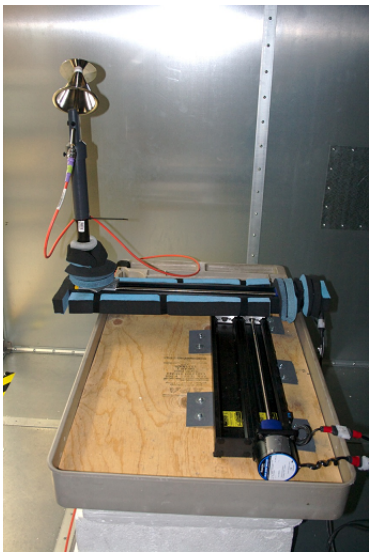

Figure 3: X-Y positioner used for platform stirring inside the ETS RC at NIST.

Instead of a wall antenna a small dual ridge horn antenna (figure 4) was used. It has the frequency range 700 MHz to 18 GHz. It was placed on a tripod at 0.8 m height and pointed towards the horizontal paddle to avoid some of its directional effects. For the correlation measurements two identical small dual ridge horn antennas were used as wall antennas.

The AUT was the same discone antenna as in the Chalmers measurement (figure 1). This was mounted on the positioner for moving around in the RC or manually moved to simulate a rotating platform.

For the correlation measurement a monopole antenna pair with center frequency of 1.9 GHz was used (figure 5). These antennas were mounted on a ground plane with separations of 0.064λ and 0.1λ.

To load the RC at NIST a number of pyramidal absorbers were used, see figure 6.

Figure 4: Small horn antenna used as wall antenna in the NIST measurements. Working at 700 MHz to 18 GHz.

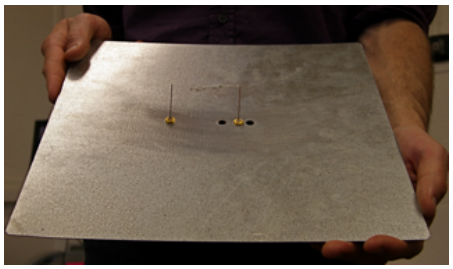

Figure 5: Monopole antennas with a center frequency of 1.9 MHz used for correlation measurements at NIST.

3.2.2 Measurement setup

The nine positions were three different orientations of the reference antenna (vertical, 45° and horizontal) at three different heights. The antenna pointed towards a side wall through out the measurements with the XY-positioner. The heights for this case were 73 cm, 100 cm, 123 cm which is spaced by more than $\lambda/2 = 21.4$ cm at 700 MHz.

The frequency band of interest for the power measurements was 500 MHz to 3 GHz, with one measurement point per MHz. In the correlation case the antennas had a more narrow band and the measurements were conducted from 1850 MHz to 1950 MHz.

The rotational plate stirrers were stepped together through 100 positions giving a total of $9 \cdot 100 = 900$ stirrer configurations for the XY-positioner and $8 \cdot 100 = 800$ stirrer configurations for the rotational case. The stepping of the plate stirrers was done with 7° and 13° steps respectively, as described in [22].

For the correlation measurement the rotational plate stirrers were stepped through 1000 positions spaced by 0.36°. This is needed to reduce the statistical error in the correlation coefficient to a sufficiently low level [21]. The rotational platform stirring was used here with 8 positions giving a total of $8 \cdot 1000 = 8000$ stirrer configurations for this measurement.

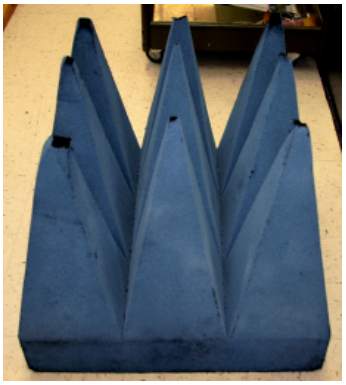

Figure 6: Pyramidal absorber used to load the RC at NIST.

Four different loading cases were measured at NIST. No damping is referred to as *Load*0, one pyramidal absorber is referred to as *Load*1, two pyramidal absorbers is referred to as *Load*2 and four pyramidal absorbers is referred to as *Load*4.

4 Results

4.1 Bluetest RTS RC at Chalmers

The RTS RC at Chalmers is an upgrade of the older HP model from Bluetest. The uncertainty for the HP RC is reported in [19]. In this section the effects of the upgrade will be presented along with a estimate for the mechanical bandwidth, B_{mech}, including the limitation of the model for a high number of stirrer positions.

4.1.1 Δf and Average K-Factor

The average mode bandwidth for the RTS RC at Chalmers is presented in figure 7. Δf is fairly constant over the frequency band 700 MHz to 3 GHz and can hence be used as a good characteristic of the amount of loading in the RC. Δf ranges from 2 MHz for the unloaded chamber to 8 MHz for the *Load*2 case.

Figure 8 shows the average K-factor, K_{av}. The amount of direct coupling is about $0.16 = 16\%$ for the unloaded chamber, about $0.2 = 20\%$ for *Load*1 and about $0.4 = 40\%$ for *Load*2. Also this quantity is fairly stable over frequency.

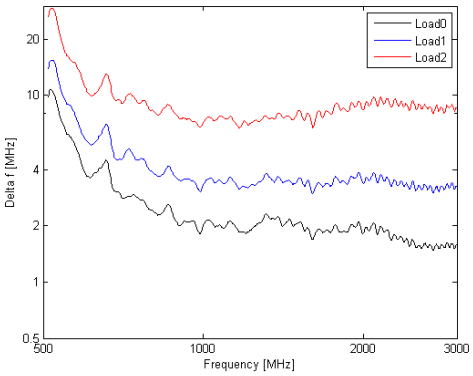

Figure 7: Average Mode Bandwidth, Δf, for the three different loading cases in the RTS RC at Chalmers. Measured and calculated from equation 18.

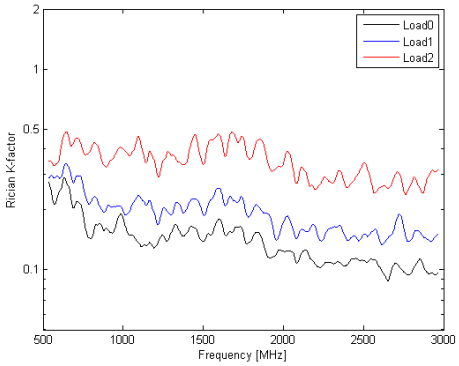

Figure 8: Average K-factor, K_{av}, for the three different loading cases in the RTS RC at Chalmers. Measured and calculated from equations 10 - 12.

4.1.2 STD Dependence on Loading and Platform Stirring

The resulting uncertainty for the upgraded chamber at Chalmers is shown in figures 9 to 12. In figure 9 the result for the unstirred case is presented. All loading cases have a lower uncertainty than previous measurements in [19] and the curves also give a much flatter frequency response.

In figure 10, full stirring is used. The lowest uncertainty is 0.14 dB and is achieved for the unloaded case for frequencies above 1500 MHz. This is also an improvement compared to previous measurements.

In both the case for the platform stirring (figure 11) and the polarization stirring (figure 12) the uncertainty is lower (better) and more stable in frequency than previous measurements (in [19]). The platform stirring has a higher influence on the uncertainty than the polarization stirring.

4.1.3 Agreement of Theoretical Uncertainty Model

In figures 13 - 15 the agreement between the experimental values and the model for uncertainty (section 2.6) is presented. The model predicts the uncertainty very well in all cases.

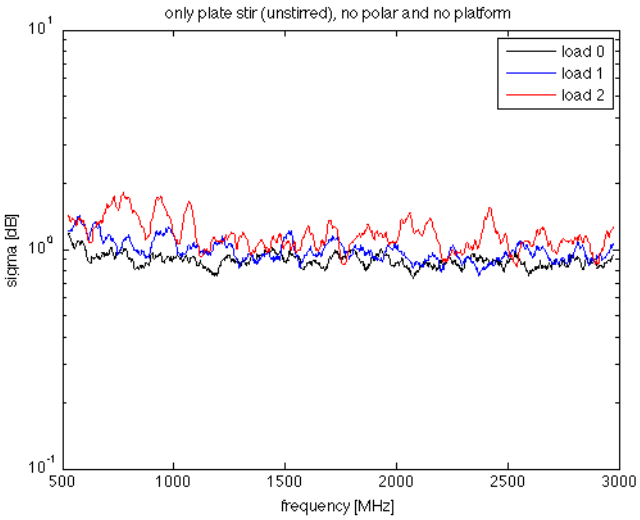

Figure 9: Measured standard deviations in upgraded reverberation chamber at Antenna Group, Chalmers. The 3 different loading cases are: empty chamber, with head phantom and head phantom and three lossy cylinders. No polarization stirring and no platform stirring is used here.

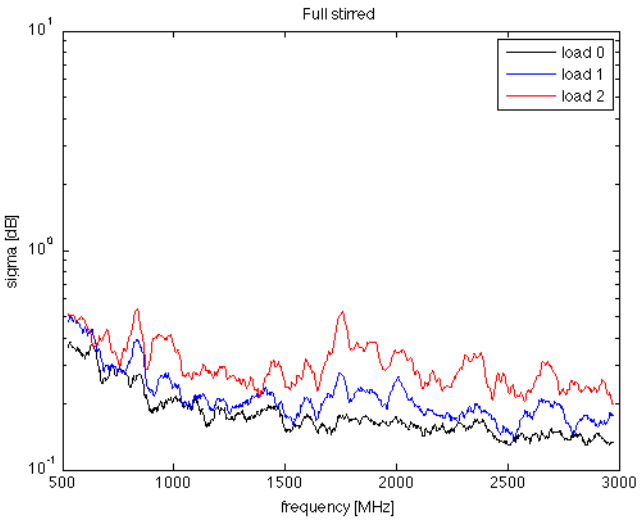

Figure 10: Measured standard deviations in upgraded reverberation chamber at Antenna Group, Chalmers. The 3 different loading cases are: empty chamber, with head phantom and head phantom and three lossy cylinders. Fully stirred with 20 platform positions and 3 orthogonal polarizations.

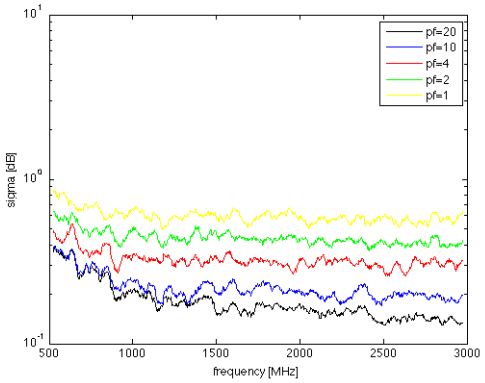

Figure 11: Measured standard deviations in upgraded reverberation chamber at Antenna Group, Chalmers. STD curves for different number of platform positions. Full polarization stirring is used.

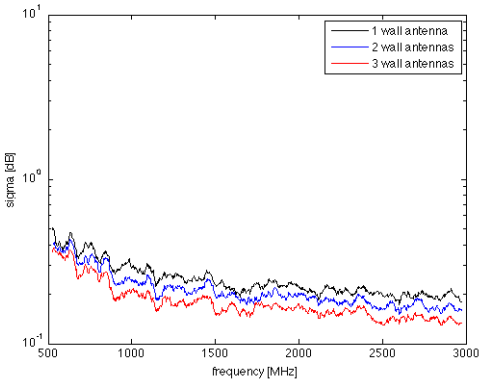

Figure 12: Measured standard deviations in upgraded reverberation chamber at Antenna Group, Chalmers. STD curves for 1, 2 and 3 wall antennas used is presented. 25 platform positions is used.

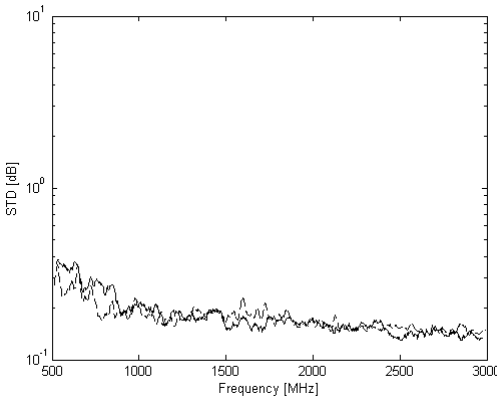

Figure 13: Measured standard deviation for RTS RC at Chalmers. Measured STD curve (solid) and modeled STD curve (dashed) for load0 with full platform stirring.

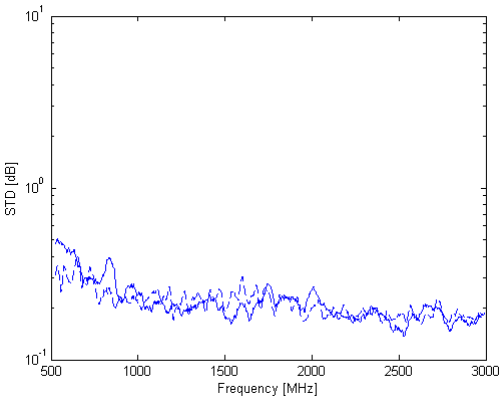

Figure 14: Measured standard deviation for RTS RC at Chalmers. Measured STD curve (solid) and modeled STD curve (dashed) for load1 with full platform stirring.

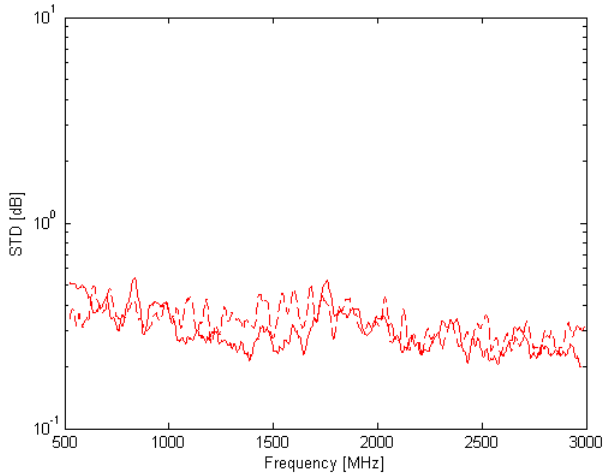

Figure 15: Measured standard deviation for RTS RC at Chalmers. Measured STD curve (solid) and modeled STD curve (dashed) for load2 with full platform stirring.

4.1.4 Extended Model Testing and a B_{mech} Estimate

When increasing the number of stirrer positions a deviation from the model starts to appear. In figures 16 and 17 the average mode bandwidth and average Rician K-factor for these measurements are presented. The average mode bandwidth is at about 2 MHz and the average Rician K-factor is about 10%.

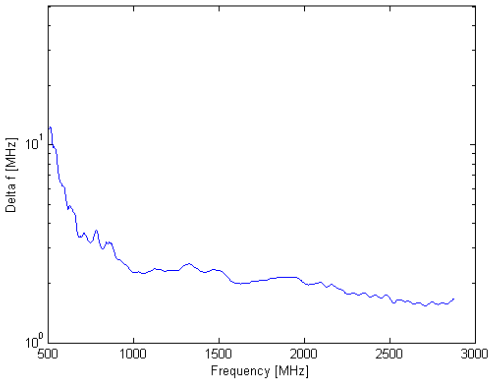

Figure 16: Average mode bandwidth, Δf, for measurements with a large number of stirrer positions in the Chalmers RC.

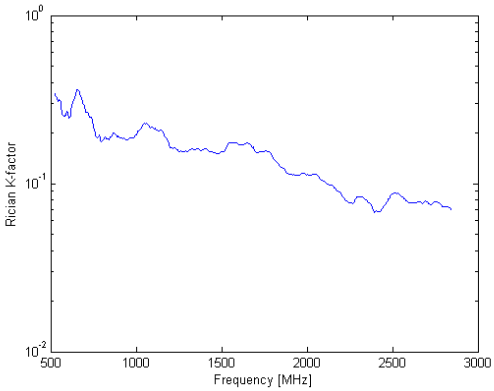

Figure 17: Average Rician K-factor, K_{av}, for measurements with a large number of stirrer positions in the Chalmers RC.

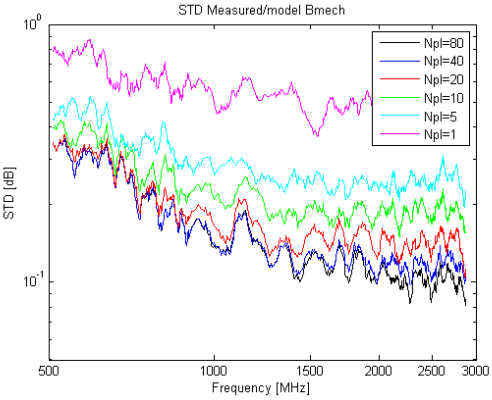

Figure 18: Standard deviation for 40 platform stirrer positions and different numbers of plate stirrer positions.

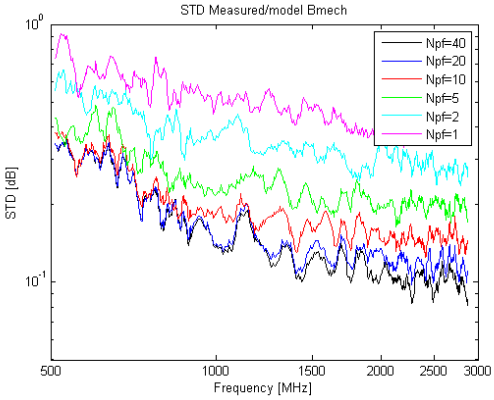

Figure 19: Standard deviation for 80 plate stirrer positions and different numbers of platform stirrer positions.

In figures 18 and 19 one can clearly see how the measured standard deviation curves gets saturated and reaches a certain value when increasing the number of stirrer positions.

B_{mech} is probably best described as a function of frequency. Although for simplicity we choose to approximate B_{mech} as fixed. This together with a somewhat unstable K_{av} led us to choose a fixed K_{av} as well in order to see how the new limitation behaves. In this early stage it is of higher importance to see the general behavior than to have a precise value.

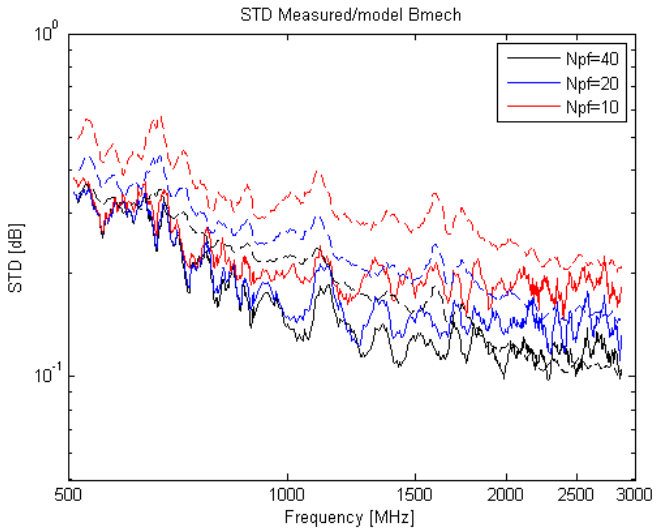

Figure 20: Measured uncertainty for 40 plate positions and varying number of platform positions. Here the original, varying K_{av} has been used.

K_{av} is set to 0.08 which is about the value for high frequencies in this case. It is also for high frequencies that the limitation kicks in and gives a difference. A plot of the case with a varying K_{av} can be seen in figure 20. This can be compared to figure 23 where a fixed K_{av} has been used.

An attempt to fit the new modified model to the measured data for a large number of stirrer positions was performed by changing B_{mech}. For 80 plate positions and 40 platform positions this resulted in a value of $B_{mech} = 20\,\text{MHz}$ and a plot of this can be seen in figure 21.

A plot of the model for different values of B_{mech} is plotted in figure 22 togeather with measured data. One can see that the agreement for 20 MHz is good and this concludes that the fit has worked well.

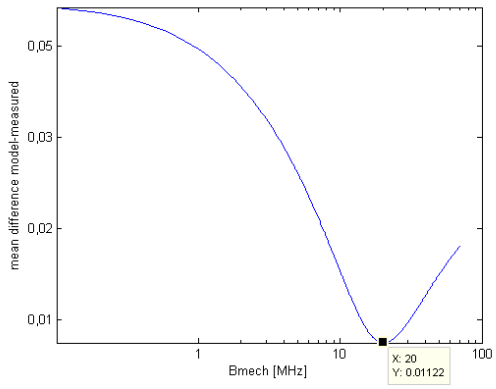

Figure 21: The mean difference between the measured data and the modified std model using B_{mech} as a function of B_{mech}. A minima is found at 20 MHz.

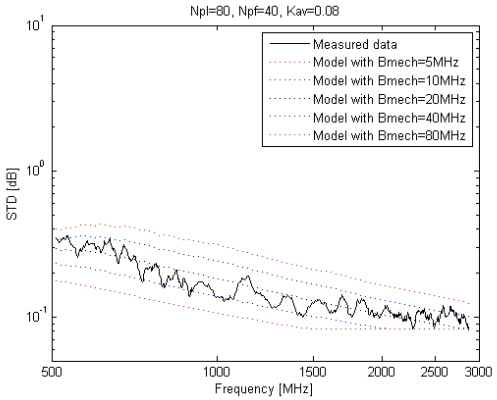

Figure 22: The B_{mech}-limited model for different values of B_{mech} together with measured results. The figure shows good agreement for $B_{mech} = 20\,\text{MHz}$.

When using this modified model together with a B_{mech} of 20 MHz the resulting graphs (figures 23 to 24) shows a good agreement between measured values and the modeled levels.

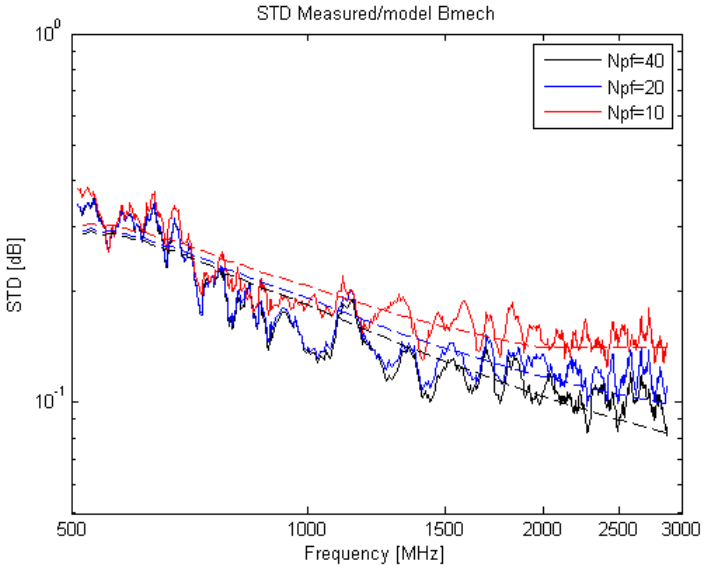

Figure 23: Measured uncertainty for 80 plate positions and 40, 20, 10 platform positions (solid lines) together with model curves from the modified model using $B_{mech} = 20\,\text{MHz}$ and $K_{av} = 0.08$ (dashed lines).

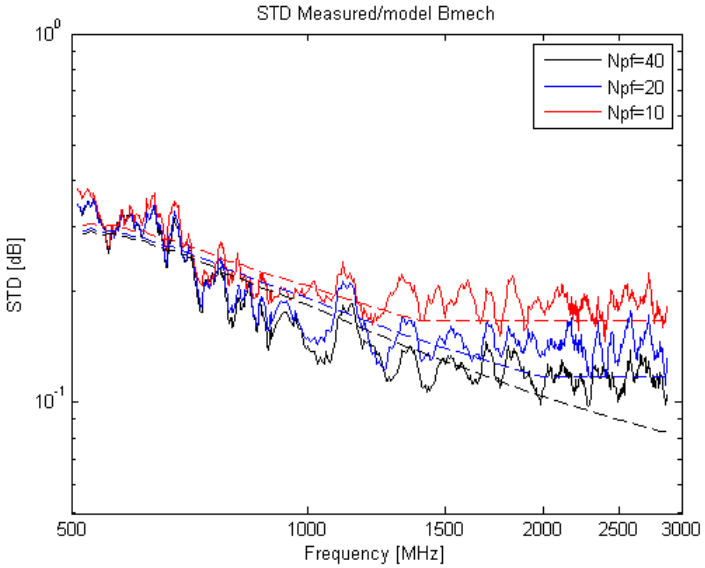

Figure 24: Measured uncertainty for 40 plate positions and 40, 20, 10 platform positions (solid lines) together with model curves from the modified model using $B_{mech} = 20\,\text{MHz}$ and $K_{av} = 0.08$ (dashed lines).

A closer look at the impact of K_{av} on the model is shown in figures 25. In figure 25 K_{av} equals zero and this corresponds to no line of sight present. In the top most curve we see both the effect of both the $N_{pf,ind}$ and $8N_{mode}$ limitations.

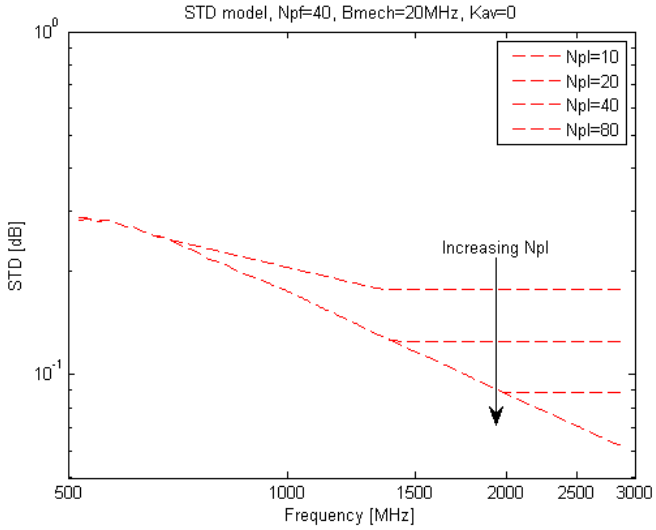

Figure 25: Model curves for different values of Npl with K_{av} equal zero. That is no line of sight. Number of platform positions are 40, $B_{mech} = 20\,\mathrm{MHz}$

The choices of the fixed values of B_{mech} and K_{av} also inpacts the model curves. Increasing B_{mech} lowers the predicted uncertainty level of the model and causes the limitation to happen for a lower frequency, see figure 26.

Increasing K_{av} gives a larger spread in the uncertainty level after the limitation has come in to play. It also changes the slope of the curve, see figure 27. A extended view of the impact of the constant average K-factor can be seen in figure 28, where the limitation is visible for three different vaules.

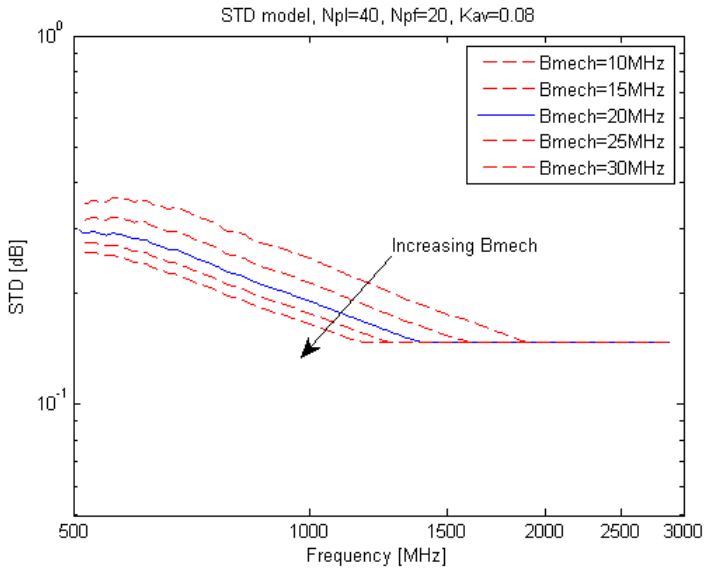

Figure 26: Model curves for different values of B_{mech} with K_{av} fixed at 0.08. Number of platform positions are 40, and number of plate positions are 80.

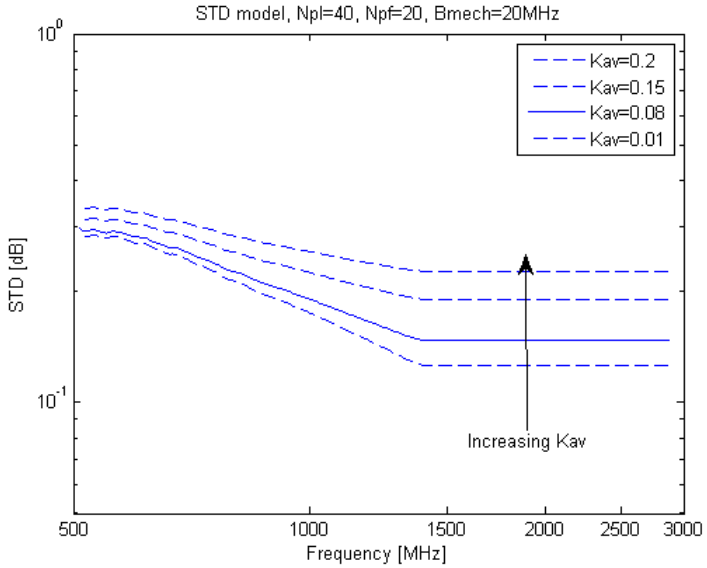

Figure 27: Model curves for different values of K_{av} with B_{mech} fixed at 20 MHz. Number of platform positions are 40, and number of plate positions are 80.

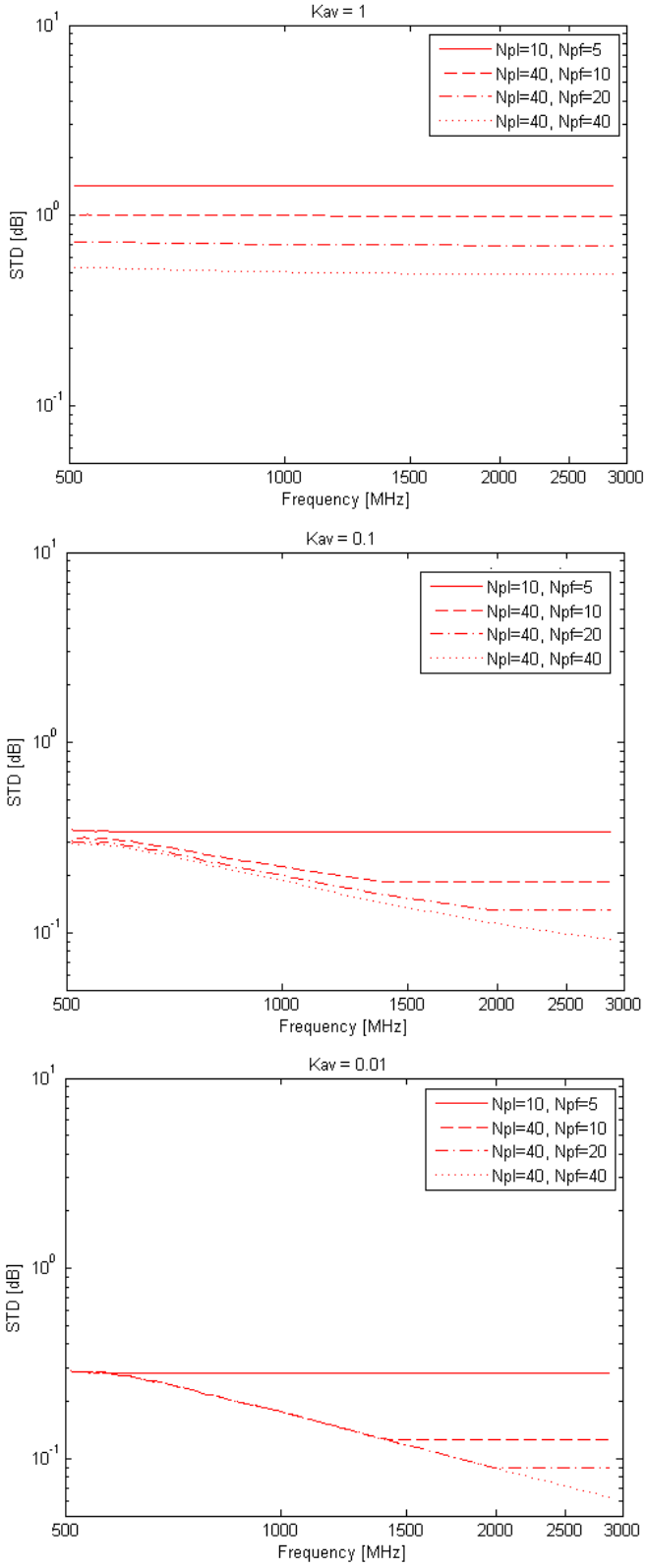

Figure 28: Model curves the B_{mech}-limited model for three different average K-factors, 1 (top graph), 0.1 (middle graph), 0.01 (bottom graph).

4.2 ETS RC at NIST

In this section the uncertainty of the ETS RC at NIST is evaluated. The influence of platform stirring and the level of agreement with the uncertainty model are main focuses here.

4.2.1 Δf and Average K-Factor

As predicted, the average mode bandwidth, Δf, is fairly constant over the frequency range. This can be seen in figure 29. For the empty (unloaded) chamber Δf is about 3 MHz and for the heavy loaded chamber (Load4) Δf is about 19 MHz.

The average K-factor is presented in figure 30. The degree of direct coupling is lower than $0.1 = 10\%$ for the unloaded chamber. It goes up to about $0.3 = 30\%$ for *Load*4.

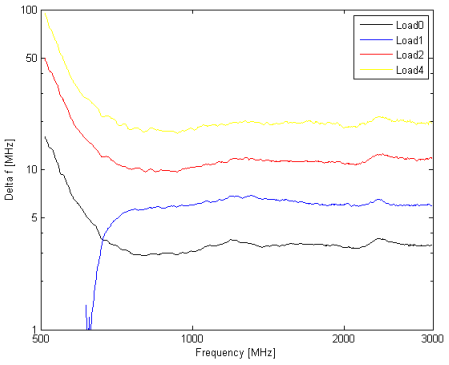

Figure 29: Average Mode Bandwidth, Δf, for the three different loading cases in the ETS RC at NIST. Measured and calculated from equation 18.

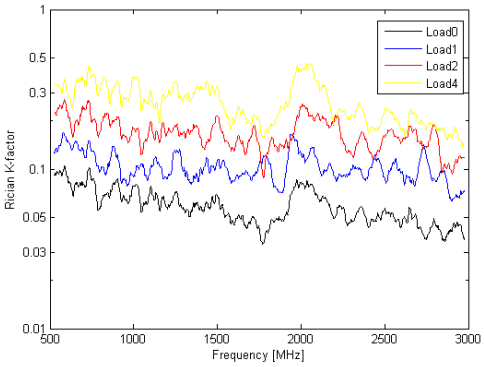

Figure 30: Average K-factor, K_{av}, for the three different loading cases in the ETS RC at NIST. Measured and calculated from equations 10 - 12.

4.2.2 Uncertainty with XY-Platform Stirring

The resulting uncertainty (standard deviation) for the ETS RC at NIST with XY-platform stirring is presented in figures 31 - 33. In figure 31 the uncertainty is presented for the four different loading cases without the use of platform stirring. In figure 32 platform stirring is used and a clear improvement can be seen.

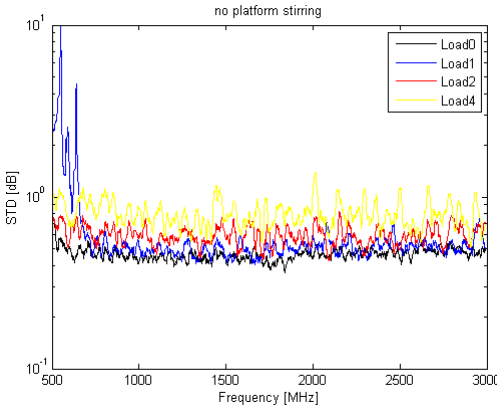

Figure 31: Measured standard deviation for ETS RC at NIST. Different loading cases are plotted without any platform stirring.

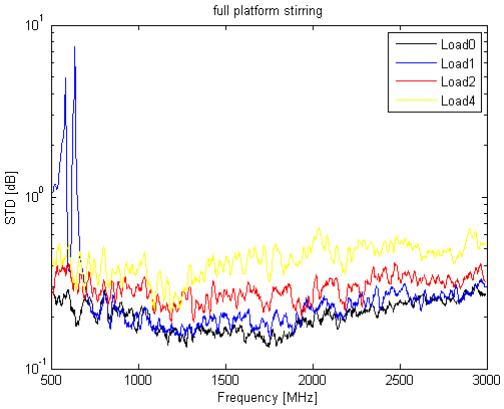

Figure 32: Measured standard deviation for ETS RC at NIST. Different loading cases are plotted with full platform stirring.

The uncertainty without platform stirring is fairly constant at about 0.5 dB for unloaded chamber (Load0). With full platform stirring (9 positions) and an unloaded chamber the uncertainty is below 0.3 dB over the whole frequency band with a minimum of 0.14 dB at around 1.75 GHz.

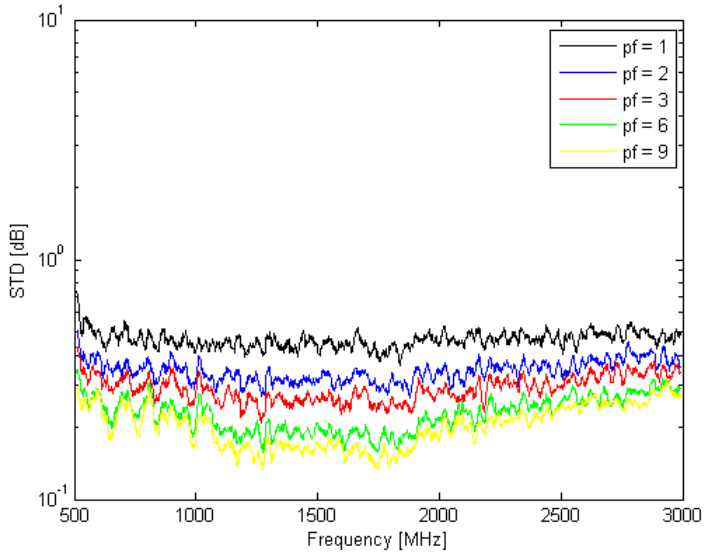

Figure 33: Measured standard deviation for ETS RC at NIST. STD curves for different number of platform positions for the Load0 case.

For the case of the unloaded chamber the dependence of uncertainty on the number of platform positions is shown in figure 33. As expected a higher number of platform positions gives lower uncertainty. For all nine platform positions, the graph becomes V-shaped – this is not present for lower number of platform positions.

In figure 34 - 37 one can see the experimental values together with the model for each of the four loading cases. The agreement is good, especially up to 2 GHz.

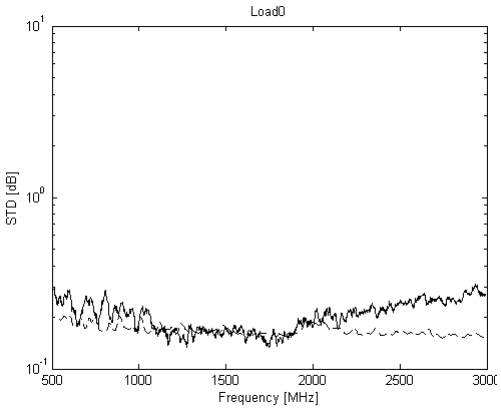

Figure 34: Measured standard deviation for ETS RC at NIST. Measured STD curve (solid) and modeled STD curve (dashed) for load0 with full platform stirring.

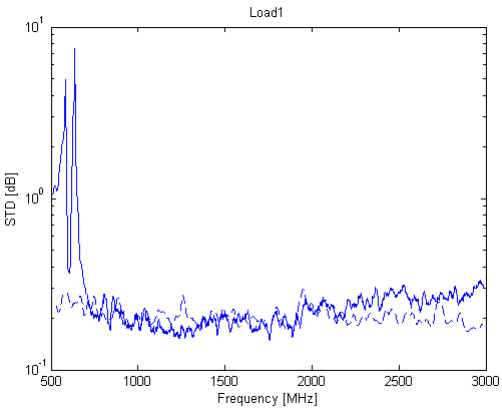

Figure 35: Measured standard deviation for ETS RC at NIST. Measured STD curve (solid) and modeled STD curve (dashed) for load1 with full platform stirring.

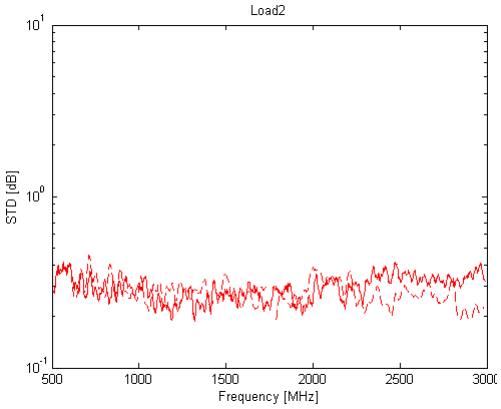

Figure 36: Measured standard deviation for ETS RC at NIST. Measured STD curve (solid) and modeled STD curve (dashed) for load2 with full platform stirring.

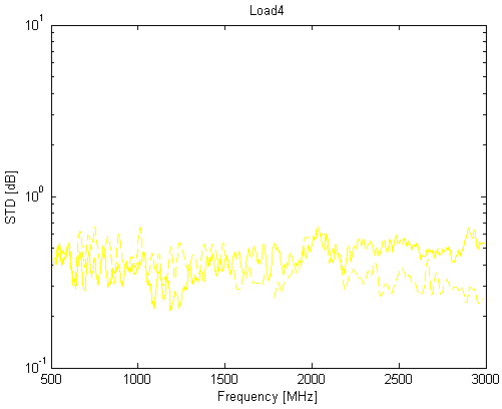

Figure 37: Measured standard deviation for ETS RC at NIST. Measured STD curve (solid) and modeled STD curve (dashed) for load4 with full platform stirring.

4.2.3 Uncertainty with Rotational Platform Stirring

When replacing the XY-positioner with a manual rotation of the antenna the absence of the XY-positioner makes for a different average mode bandwidth and a different average K-factor. Δf drops down to 1.1 MHz and K_{av} becomes 2% for $load0$, this can be seen in figure 38 and 39. The level of loading is less now that the lossy positioner is no longer present in the chamber.

In figure 40 the uncertainty is shown for different number of platform positions. In comparison to the XY-platform stirring in figure 33 the rotational platform stirring gives lower uncertainty and a flatter frequency response.

The uncertainty for the ETS RC at NIST with rotational platform stirring is presented in figure 41 and 42. The graph shows the standard deviation for the chamber together with the uncertainty model (dashed line). The agreement between the model and experimental values are good over the whole frequency band and gives a even better result than the measurement with the XY-positioner.

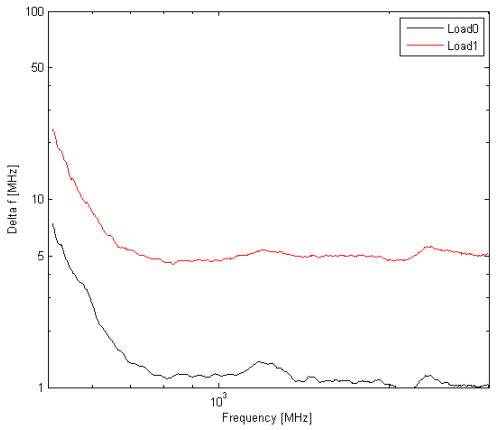

Figure 38: Average Mode Bandwidth, Δf, for two different loading cases in the ETS RC at NIST with rotating platform stirring. Measured and calculated from equation 18.

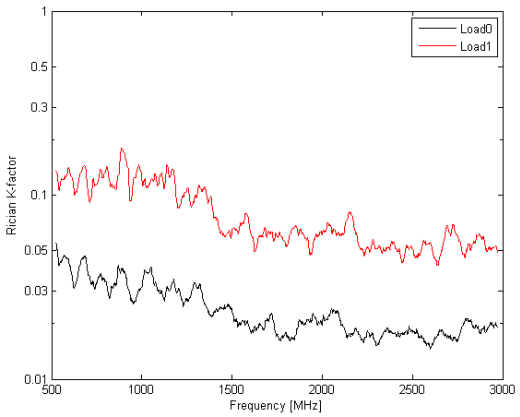

Figure 39: Average K-factor, K_{av}, for two different loading cases in the ETS RC at NIST with rotating platform stirring. Measured and calculated from equations 10 - 12.

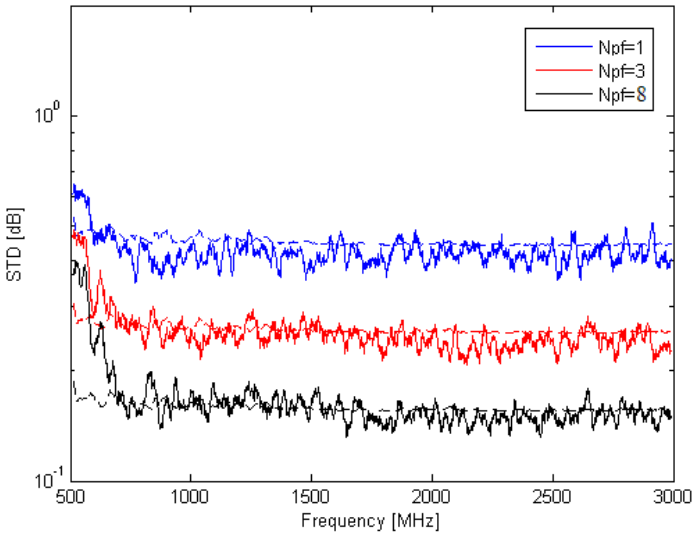

Figure 40: Measured standard deviation for ETS RC at NIST. STD curves for different number of platform positions for the Load0 case with rotating platform stirring. Dashed curves is the modeled STD-levels.

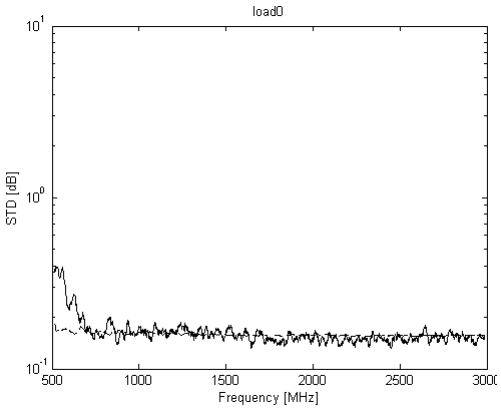

Figure 41: Measured standard deviation for ETS RC at NIST with rotating platform stirring. Measured STD curve (solid) and modeled STD curve (dashed) for load0 with full platform stirring.

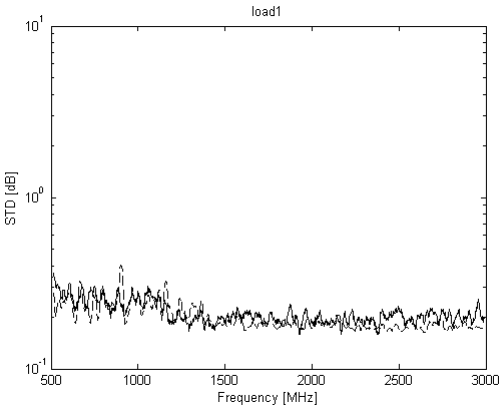

Figure 42: Measured standard deviation for ETS RC at NIST with rotating platform stirring. Measured STD curve (solid) and modeled STD curve (dashed) for load1 with full platform stirring.

4.2.4 High K_{av} Investigation for Rotational Platform Stirring

To further investigate the rotational platform stirring a test with the horn antenna pointed directly at the AUT was conducted. This increases the K_{av}-factor and is sort of a worst case scenario, as a low direct coupling component is desirable.

In figure 43 the resulting average K-factor is shown for this worst case scenario. Even though the direct path should be strong the K_{av} stays low. This can be due to the rotation of the AUT which distributes the polarization over 360°.

In figure 44 the standard deviation for different number of platform positions are presented. The curves shows a small increase in standard deviation/uncertainty compared to when the horn was pointed at the stirrer. The increase is very small and this is another indication that the rotational platform is a effective stirrer for these types of measurements.

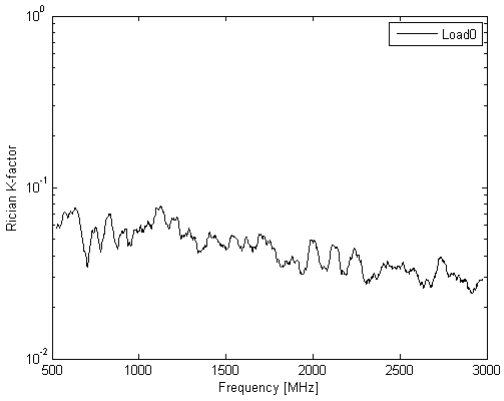

Figure 43: Average K-factor, K_{av}, with the horn pointed towards the AUT. Measured with rotational platform stirring.

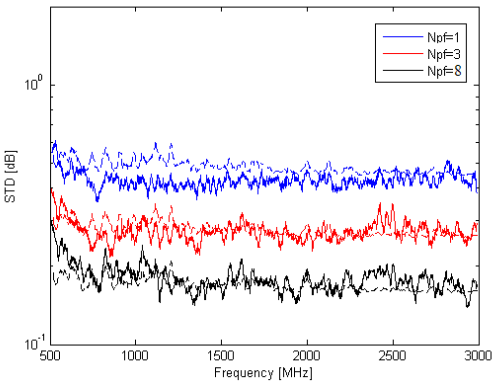

Figure 44: Measured standard deviation for ETS RC at NIST with the horn pointed towards the AUT. STD curves for different number of platform positions for the Load0 case with rotating platform stirring.

4.2.5 Correlation as a Uncertainty Measure

The two antenna separations has the corresponding correlations coefficients of around 0.82 for a separation of 0.064λ and around 0.68 for a separation of 0.1λ. Measurement results for one position and orientation are presented in figures 45 and 46. The two curves in each figure corresponds to correlation coefficients with two different, orthogonally polarized transmit antennas.

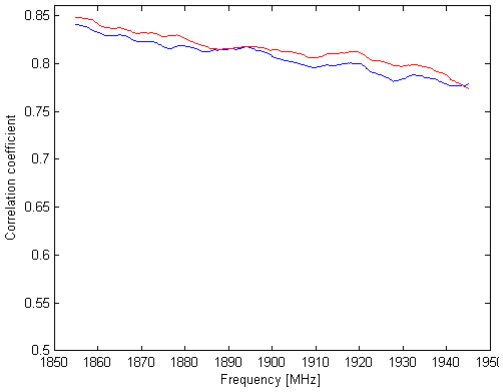

Figure 45: Correlation coefficient for measurement on monopole antenna pair with a separation of 0.064λ. Two different curves from two orthogonally polarized transmit antennas.

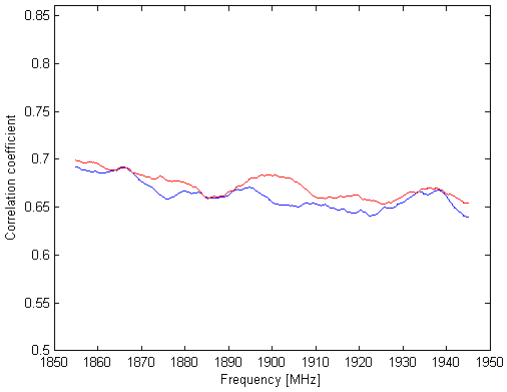

Figure 46: Correlation coefficient for measurement on monopole antenna pair with a separation of 0.1λ. Two different curves from two orthogonally polarized transmit antennas.

The standard deviation of the correlation coefficient for the nine different positions and orientations of the monopole antenna pair are presented in figures 47 and 48. The figures shows standard deviation as a function of frequency with different number of plate stirrer positions. For the maximum number of positions ($N_{pl} = 1000$) the standard deviation becomes around 0.10 dB for the 0.064λ separation and around 0.14 dB for the 0.1λ separation.

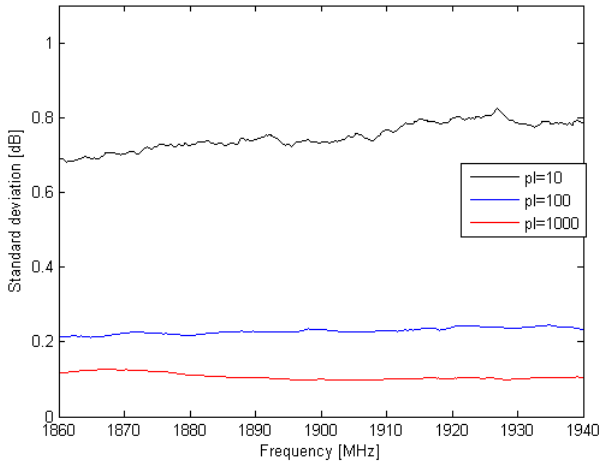

Figure 47: Standard deviation correlation coefficients of nine measurements on monopole antenna pair with a separation of 0.064λ. Result are presented as a function of number of plate stirrer positions.

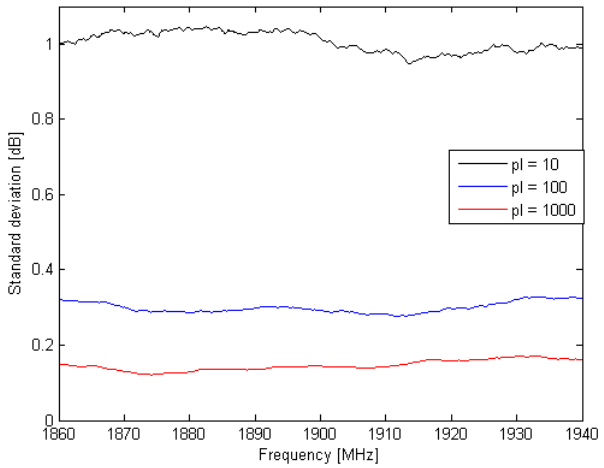

Figure 48: Standard deviation correlation coefficients of nine measurements on monopole antenna pair with a separation of 0.1λ. Result are presented as a function of number of plate stirrer positions.

5 Discussion

The uncertainty in the two different chambers can be compared to assess the best performance of the two. On the other hand the loading is different between the RC's, as one can see from looking at the average mode bandwidth, Δf. So the uncertainty graphs with loading dependence have to be assessed individually as, for instance, *Load*1 means different things for the RTS RC and for the NIST RC. It also means different things for the two different types of platform stirring in the NIST RC, as the XY-platform adds quite a bit of loading in itself.

5.1 RTS RC at Chalmers

A brief note about the measurement setup is given here. It is of importance to setup the AUT on the platform within a certain height. If the antenna is placed too high in relation to the shielding screen the reference transfer function becomes too low resulting in a poor uncertainty value. In this case the screen height is 99 cm and placing the AUT at a height of 108 cm gives low uncertainty while a height of 112 cm is too high and gives poor measurement performance. Measurement results and a detailed sketch of the setup is given in appendix A.

5.1.1 Effects of the Upgrade on the Uncertainty

The improvements made to the RC reduces the direct coupling, the K_{av}-factor, compared to the previous version. This gives the necessary conditions for a over all reduction of the uncertainty. The addition of a screen enables this but the positioning of the chamber antennas close together reduces the space diversity that used to be present. This gives the cause for changes in the model where the antennas are seen only as one for the line of sight part. Still with this disadvantage the overall uncertainty is lowered so the trade off gives a positive effects.

The model, including the modification of number of antennas for the line of sight part, predicts the uncertainty very well for all loading cases measured. At least for these lower number of stirrer positions of maximum 20 plate positions and 25 platform positions.

Polarization stirring did not have as much influence on uncertainty as platform stirring had. The platform provides a sort of polarization averaging when rotating in the chamber. This might result in a smaller effect of the polarization stirring when this is already partly done by the platform. The platform also adds a number of positions, giving more mode configurations in the chamber to be used for averaging.

5.1.2 Modified Uncertainty Model and B_{mech} Estimate for High Number of Stirrer Positions

When increasing the number of stirrer positions to a very high number the original model is not as accurate any more. The proposed method to determine the number of excited modes, N_{mode}, in equation 22 provides one possible way to deal with this problem.

The original uncertainty model (eq 20) has a physical foundation. In order to apply it to the conditions of a high number of stirrer positions some less physical simplifications had to be made. This is still an early stage of trying to understand the mechanisms in play and care is taken to make the model work for these conditions before finding a physical explanation.

A fixed value for B_{mech} is assumed. This works quite well for the present conditions and a reasonable value is found. However, what actually determines the mechanical bandwidth is not investigated in this report. It should contain stirrer shapes and sizes, stirrer sequences, frequency among other things but the actual form of this is left for future studies.

Also a fixed K_{av} is used in this modified approach. The fixed value is taken from the higher end of the frequency band (see figure 17) where the limitation of the model is the most important. Without this fixed value the higher K_{av} for lower frequencies results in a to high uncertainty prediction of the model, as the average K-factor is what's limiting the model there.

5.2 ETS RC at NIST

5.2.1 Uncertainty with XY-Platform Stirring

In the graphs including *Load*1 a strange behavior can be seen for frequencies lower than 700 MHz. This is the result of a bad cable used in that measurement, the other loading cases was made with a replacement cable in place. A new measurement of that loading case has not been possible to perform due to a tight schedule in the RC. This being said, the behavior above 700 MHz looks reasonable and in line with the other loading cases.

The average mode bandwidth also has a large increase below 700 MHz for all loading cases. This can be due to the effect of the directivity and cut-off frequency of the horn antenna. This could be compensated for by measuring the directivity of the horn in the anechoic chamber, although due to time limitations this has not been possible.

The unloaded chamber and *Load*1 uncertainty curves in figure 34 and 35 have a slight V-shape, increasing over 1.75 GHz. This is not expected – the uncertainty should be fairly stable over frequency with a slight decrease for higher frequencies. The curves are flat for the unstirred case in figure 31 and the dependence of the platform stirring is seen in figure 33.

The V-shape appears for higher number of platform positions indicating a potential problem with correlation between platform positions. High correlation would mean that part of the same signal is measured on different positions giving a false low standard deviation (false low uncertainty). The correlation follows a sinc function and high correlation might have appeared for 1.75 GHz under present circumstances.

5.2.2 Uncertainty with Rotational Platform Stirring

When adding a rotation instead of XY-translation it is clear from figure 40 that the problem with correlation disappear. The curves are flat over frequency and follow the model very well. The lower uncertainty compared to the XY-positioner might be due to the lower loading of the RC here. Although the K_{av}-factor drops down and this is another reason that the standard deviation is lower in this case. The direct path is reduced by the polarization equalization performed by the rotation. Only two loading cases have been measured and it would be interesting to see how this platform stirring would perform for higher loading.

The test with the high K_{av} turned out to be not as high as expected. The rotation of the antenna helps keeping the average K-factor down even when the antennas is

pointed towards each other. This average K-factor is a good way of dealing with the K-factor and together with a rotational platform it gives good measurement performance.

5.2.3 Uncertainty Estimate Using the Correlation Coefficient

The standard deviation or uncertainty is at about the same level for the correlation measurement as for the power measurement. In both cases it goes down to about 0.14 dB for maximum number of stirrer positions. A more fair comparison is to use the same number of samples for each case, the power measurement uncertainty was used with 100 plate stirrer positions and this corresponds to the middle curve (the blue curve) in figures 47 and 48. Now the standard deviation in the correlation case is around 0.23 dB for the 0.064λ case and around 0.29 dB for the 0.1λ case. To compare to 0.15 dB for the power measurement uncertainty.

The uncertainty depends in this case on chamber loading, number of stirrer positions, type of platform stirring and in addition; correlation coefficient. It would have been interesting to see how large of deviation in uncertainty a even longer antenna separation (lower correlation coefficient) would have given. This could be investigated in a future study, along with relation to loading of the RC to try to establish a model for the correlation dependence on uncertainty.

6 Conclusion

The upgrade of the Bluetest RTS RC is an improvement. The average mode bandwidth as well as the Rician K-factor is lower than in the HP RC. This means that a lower total uncertainty can be achieved. Uncertainty as low as 0.14 dB has been measured for an unloaded chamber above 1.5 GHz.

The model works well for this upgrade when accounting for that the wall antennas are located in the same physical position, reducing the space diversity but still gaining in uncertainty through a lower average K-factor.

A estimate of the mechanical bandwidth of the Bluetest RST RC has been determined to be 20 MHz. Using this value together with Weyl's formula as a limiting level in the uncertainty model gives a reasonable fit to measured data. Although it is not perfect and further studies are needed to understand this aspect more thoroughly.

For the B_{mech} estimation a AUT setup with vertical, 45° and horizontal antenna were used. This differed a little from the initial setup with a vertical, a tangential

horizontal and a radial horizontal AUT were used. This difference is of minor importance and no clear difference in the measured uncertainty has been noticed.

For the RC at NIST, the addition of a XY-platform stirrer has improved the overall uncertainty. A uncertainty below 0.3 dB is measured with the platform in place. However, the platform introduces some correlation effects, which affect the uncertainties frequency response. A correlation peak can be seen for 1.75 GHz with more than seven platform positions, giving a lower uncertainty value than actually what is present.

When changing the XY-platform to a rotational platform for the RC at NIST the uncertainty improves even more, down to 0.15 dB. The problem with correlation disappear and the frequency response is more flat. In this case a lower loading of the RC is also achieved, this is useful to have more control over the amount of loading in the RC.

The uncertainty model from Prof. Kildal's group at Chalmers uni. describes the uncertainty in the NIST chamber well. In the case with a rotational platform the model works fine for all of the measured frequency bands. This RC differs from the RC at Chalmers both in size (the NIST RC is 13 times larger) and in terms of stirring mechanisms (shape and type of mode stirrers). The fact that the model works for both of them is a good indication that the model really can describe how reverberation chambers performs in terms of uncertainty.

References

[1] N. Olano, C. Orlenius, K. Ishimiya, and Z. Ying, "WLAN MIMO throughput test in reverberation chamber," in *Antennas and Propagation Society International Symposium, 2008. AP-S 2008. IEEE*, pp. 1–4, 2008.

[2] K. Madsén, P. Hallbjörner, and C. Orlenius, "Models for the Number of Independent Samples in Reverberation Chamber Measurements With Mechanical , Frequency , and Combined Stirring," *IEEE Antennas and Wireless Propagation Letters*, vol. 3, no. 1, pp. 48–51, 2004.

[3] D. A. Hill, "Boundary Fields in Reverberation Chambers," *IEEE Transaction on Electromagnetic Compatibility*, vol. 47, no. 2, pp. 281–290, 2005.

[4] P. Corona, J. Ladbury, and G. Latmiral, "Reverberation-Chamber Research — Then and Now : A Review of Early Work and Comparison With Current Understanding," *IEEE Transaction on electromagnetic compatibility*, vol. 44, no. 1, pp. 87–94, 2002.

[5] C. L. Holloway, D. A. Hill, J. Ladbury, P. Wilson, G. Koepke, and J. Coder, "On the Use of Reverberation Chambers to Simulate a Rician Radio Environment for the Testing of Wireless Devices," *IEEE Transactions on Antennas and Propagation*, vol. 54, pp. 3167–3177, Nov. 2006.

[6] K. Rosengren and P.-S. Kildal, "Study of distributions of modes and plane waves in revermeration chambers for the characterization of antennas in a multipath environment," *Microwave and Optical Technology Letters*, vol. 30, no. 6, pp. 386–391, 2001.

[7] H. Fielitz, K. A. Remley, C. L. Holloway, Q. Zhang, Q. Wu, and D. W. Matolak, "Reverberation-Chamber Test Environment for Outdoor Urban Wireless Propagation Studies," *IEEE Antennas and Wireless Propagation Letters*, vol. 9, pp. 52–56, 2010.

[8] P.-S. Kildal and C. Orlenius, "TRP and TIS / AFS Measurements of Mobile Stations in Reverberation Chambers (RC)," *CTIA Certification Program Working Group Contribution*, pp. 1–36, 2009.

[9] X. Chen, P.-S. Kildal, C. Orlenius, and J. Carlsson, "Channel Sounding of Loaded Reverberation Chamber for Over-the-Air Testing of Wireless Devices: Coherence Bandwidth Versus Average Mode Bandwidth and Delay Spread," *IEEE Antennas and Wireless Propagation Letters*, vol. 8, pp. 678–681, 2009.

[10] P.-S. Kildal, X. Chen, C. Orlenius, M. Franzen, and C. S. Patane L, "Characterization of Reverberation Chambers for OTA Measurements of Wireless Devices : Physical Formulations of Channel Matrix and new Uncertainty

Formula," *accepted for publication in IEEE Transaction on Antennas and Propagation*, 2012.

[11] J. Kostas and B. Boverie, "Statistical model for a mode-stirred chamber," *IEEE Transactions on Electromagnetic Compatibility*, vol. 33, no. 4, pp. 366–370, 1991.

[12] R. R. Lentz and H. C. Anderson, "Reverberating chamber for EMC measurements," in *Proceedings EMC Symposium*, pp. 446 – 451, 1979.

[13] H. T. Friis, "Friis Transmission Equation," in *IRE proceedings*, vol. 34, p. 254, 1946.

[14] D. A. Hill, T. M. Ma, A. R. Ondrejka, B. F. Riddle, M. L. Crawford, and R. T. Johnk, "Aperture Excitation of Electrically Large , Lossy Cavities," *IEEE Transactions on Electromagnetic Compatibility*, vol. 36, no. 3, pp. 169–178, 1994.

[15] D. A. Hill, "Plane Wave Integral Representation for Fields in Reverberation Chambers," *IEEE Transaction on Electromagnetic Compatibility*, vol. 40, no. 3, pp. 209–217, 1998.

[16] U. Carlberg, P.-S. Kildal, and J. Carlsson, "Study of antennas in reverberation chamber using method of moments with cavity Green's function calculated by Ewald Summation," *IEEE Transaction on Electromagnetic Compatibility*, vol. 47, no. 4, pp. 805–814, 2005.

[17] K. Rosengren and P.-S. Kildal, "Radiation efficiency, correlation, diversity gain and capacity of a six-monopole antenna array for a MIMO system: theory, simulation and measurement in reverberation chamber," *Microwaves, Antennas and Propagation, IEE Proceedings*, vol. 152, no. 1, pp. 7–16, 2005.

[18] X. Chen and P.-S. Kildal, "Frequency-Dependent Effects of Platform and Wall Antennas on Measurement Uncertainty in Reverberation Chamber," in *Antennas and Propagation (EuCAP)*, no. 2, pp. 1–3, 2010.

[19] P.-S. Kildal, S.-H. Lai, and X. Chen, "Direct Coupling as a Residual Error Contribution During OTA Measurements of Wireless Devices in Reverberation Chamber," in *IEEE AP-S International Symposium on Antennas and Propagation*, (Gothenburg, SWEDEN), pp. 8–11, 2009.

[20] K. Rosengren, *Characterization of Terminal Antennas for Diversity and MIMO Systems by Theory, Simulations and Measurements in Reverberation Chamber*. PhD thesis, Chalmers University of Technology, 2005.

[21] P. Hallbjorner, "Accuracy in Reverberation Chamber Antenna Correlation Measurements," in *International workshop on Antenna Technology: Small*

and Smart Antennas Metamaterials and Applications, pp. 170–173, IEEE, Mar. 2007.

[22] C. S. Patane L, "Reverberation Chamber Performance and Methods for Estimating the Rician K-factor," tech. rep., Chalmers University of Technology, 2010.

A Measurement Issues for High Placement of the AUT

When doing measurements in the RC at Chalmers I've encountered some problems that are presented here. Placing the AUT too high in the RC leads to a degrading in performance in terms of uncertainty. In figure 49 it is clear that the reference transfer function for the highest height deviates from the rest of the measurements in a consistent way. This leads to a high standard deviation and a high uncertainty. When placing the AUT at an appropriate height this effect is not visible, see figure 50.

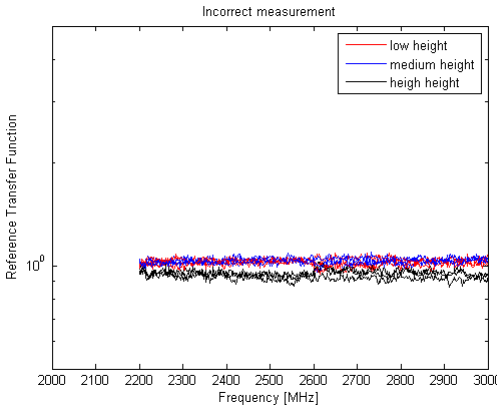

Figure 49: Reference transfer function for the nine different orientations of the AUT. Measurement done with incorrect height 112 cm causes a wide spread and results in a high standard deviation (high uncertainty).

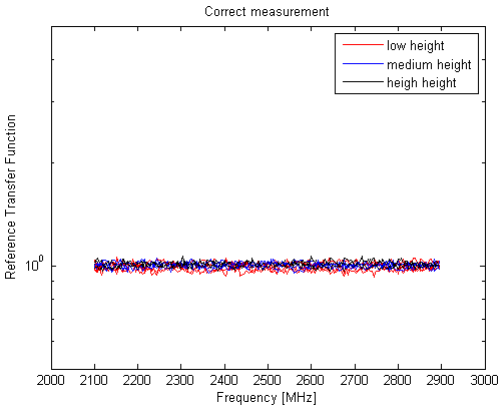

Figure 50: Reference transfer function for the nine different orientations of the AUT. Measurement done with a appropriate height 108 cm gives a small spread and results in a low standard deviation (low uncertainty).

In figure 51 a sketch of the measurement setup is provided to show more precise where these problems occurred. The screen height is 99 cm and placing the AUT at a height of 108 cm gives low uncertainty while a height of 112 cm is too high and gives poor measurement performance in this RC under these geometrical conditions.

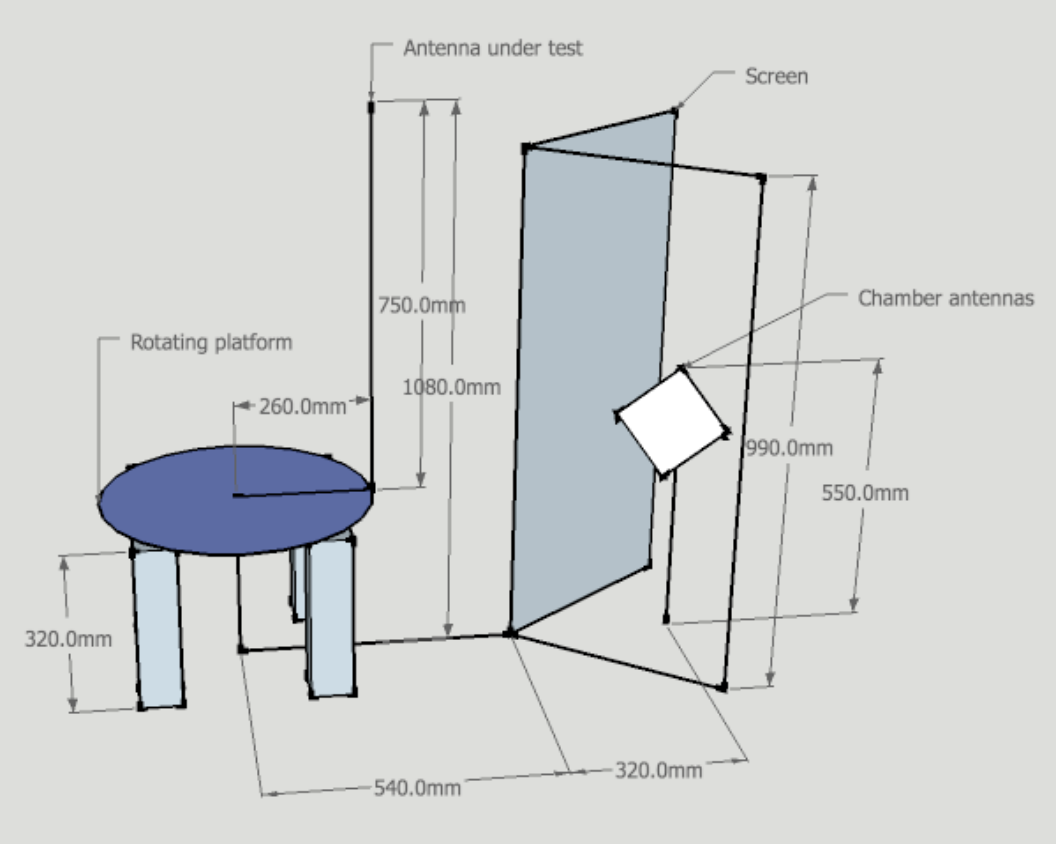

Figure 51: Sketch over the measurement setup with the height that gave good measurement performance. If the AUT was placed 4 cm higher a degrading in performance was measured.